nature portfolio

https://doi.org/10.1038/s41566-021-00880-1

Supplementary information

Synthetic helical dichroism for six-dimensional optical orbital angular momentum multiplexing

In the format provided by the authors and unedited

Supplementary information for:

Synthetic Helical Dichroism for Six-Dimensional Optical Orbital Angular Momentum Multiplexingt

Xu Ouyang,[1,2]† Yi Xu,[2,8]† Mincong Xian[2], Ziwei Feng[2], Linwei Zhu,[3] Yaoyu Cao,[1] Sheng Lan,[4] Bai-ou Guan,[1] Cheng-Wei Qiu,[5] Min Gu[6,7*], and Xiangping Li[1*]

[1] *Guangdong Provincial Key Laboratory of Optical Fiber Sensing and Communications, Institute of Photonics Technology, Jinan University, Guangzhou, China.*

[2] *Department of Electronic Engineering, College of Information Science and Technology, Jinan University, Guangzhou, China.*

[3] *School of Physics and Optoelectronic Engineering, Ludong University, Yantai, China.*

[4] *Guangdong Provincial Key Laboratory of Nanophotonic Functional Materials and Devices, School of Information and Optoelectronic Science and Engineering, South China Normal University, Guangzhou, China.*

[5] *Department of Electrical and Computer Engineering, National University of Singapore, Singapore, Singapore.*

[6] *Institute of Photonic Chips, University of Shanghai for Science and Technology, Shanghai, China.*

[7] *Centre for Artificial-Intelligence Nanophotonics, School of Optical-Electrical and Computer Engineering, University of Shanghai for Science and Technology, Shanghai, China.*

[8] *Present address: Advanced Institute of Photonics Technology, School of Information Engineering, Guangdong University of Technology, Guangzhou, China.*

†These authors contributed equally to this work.

[*] *Corresponding authors: gumin@usst.edu.cn, xiangpingli@jnu.edu.cn*

Supplementary notes:

Supplementary note 1. Definition of synthetic helical dichroism

Similar to the conventional definition of dichroism OAM-D in Ref. [1], we define the synthetic helical dichroism (HD) of a nanostructure under the excitation of OAM beams with opposite topological charges while the same wavelength and linear polarization as:

$$\Delta\sigma^{HD}_{\pm|\ell|,\, p,\, \lambda} = \sigma^{HD}_{+|\ell|,\, p,\, \lambda} - \sigma^{HD}_{-|\ell|,\, p,\, \lambda} \qquad (1)$$

where σ is linear absorption power of a nanostructure under the excitation of a tightly focused OAM beam with a specified combination of topological charge (ℓ), linear polarization (p) and wavelength (λ). Since the OAM beams are tightly focused, therefore their focus spots with different topological charges ($|\ell|$) have longitudinal components which are overlapped in space. At the same time, as the size of the disordered nanostructures we used in this paper is in deep subwavelength scale, i.e. with averaged diameter 8 nm and length 30 nm, there are more than 4000 coupled GNRs inside a focal spot (λ~800 nm). It means that the aforementioned synthetic HD can be generalized to the $\Delta\sigma^{HD}_{\ell_m,\, \ell_n,\, p,\, \lambda}$ accounting for the light-matter interaction of tightly focused OAM beams with topological charges of any absolute values while the same wavelength and linear polarization:

$$\Delta\sigma^{HD}_{\ell_m,\, \ell_n,\, p,\, \lambda} = \sigma^{HD}_{\ell_m,\, p,\, \lambda} - \sigma^{HD}_{\ell_n,\, p,\, \lambda} \qquad (2)$$

Supplementary note 2. Polarization ellipse mediated synthetic helical dichroism

The tight focusing of OAM beam generally leads to longitudinal field (E_z) with nontrivial intensities and transverse field (E_x and E_y). The longitudinal and transverse components have spatially-variant amplitudes as well as phase shifts along both the transverse and propagation directions (Supplementary Fig. 1). The superposition of such longitudinal field and transverse field leads to a tilted polarization ellipse at certain *X-Z* and *Y-Z* planes (Supplementary Figs. 2 and 3). The inclination angle (α_e) of the polarization ellipse in the *X-Z* plane can be expressed as

$$\tan(2\alpha_e) = \frac{2E_xE_z cos\varphi}{E_x^2 - E_z^2} \qquad (3)$$

where E_x and E_z represent transverse and longitudinal field components, respectively, which can be calculated following Eqs. 1-3 shown in Numerical Methods. $\delta_{zx}(x,y,z) = Arg\big(E_z(x,y,z)\big) - Arg\big(E_x(x,y,z)\big)$ denotes the OAM-dependent Gouy phase difference between the two field components. Similarly, the inclination angle in other planes can also be calculated following Eq. 3. Consequently, the rotation of polarization ellipses within the focal volume is spatially-variant in both transverse and propagation directions, which shows distinct distributions by beams of different topological charges. To illustrate the OAM-dependent polarization ellipse, Supplementary Fig. 2 shows the distinct Gouy phase differences along the propagation direction for two lines when $X = Y = 100$ nm and $X = Y = 300$ nm for OAM beams (ℓ =

±1 and $\ell = \pm 3$), respectively. The distributions of polarization ellipses in the *X*-*Z* plane are shown in Supplementary Fig. 2c. Supplementary Fig. 3 further elaborates the rotation of polarization ellipses in *X*-*Y*, *X*-*Z* and *Y*-*Z* planes for OAM beams with different topological charges.

When focused OAM beams engage with an achiral nanoparticle whose geometric center located at the spatial position where the polarization ellipses (or the ellipse inclination angle) are distinct under the excitation of OAM beams with different topological charges, the achiral nanoparticle can exhibit distinct excitation strengths (or optical absorption) for synthetic HD. Supplementary Fig. 4 illustrates the calculated inclination angle difference of the polarization ellipses by focusing OAM beams with opposite topological charges ($\ell = \pm 1$). The rotated polarization ellipse plays an important role in excitation of a GNR with different strengths. In Supplementary Fig. 5, the linear optical absorption powers in such a GNR reveals a difference for synthetic HD not only for OAM beams with opposite topological charges but also different absolute topological charges.

When focused OAM beams engage with disordered nanoaggregates, the presence of strong coupling among these plasmonic nanoparticles induces hotspots with remarkably augmented local fields. The appearance of near-field hotspots can enhance the local field by orders of magnitude. As a result, the strength of synthetic HD generally weak in isolated single nanoparticles due to size mismatch between the nanoparticles and helical wavefronts can be resonantly enhanced by orders of magnitude originated from the hotspot effect.

Supplementary note 3. Physical processes during optical encoding and decoding by focused OAM beams

Because there are thousands of disordered coupling GNRs inside a focal spot, the macroscopic signal collected from the focal spot will manifest itself as statistical properties which could be regarded as ensemble average effects over all constituent GNRs in the assemble. Although GNRs in the nanoaggregate sustain different HD responses one from the other due to strong disorder effects, HD defined as the difference in absorption powers inside individual nanoparticles is hardly to be perceivable (Fig. 3, e and g-i) before optical encoding through the photothermal deformation effect. Empowered by the amplified HD due to the hotspot effect, the absorption can heat up a population of GNRs near the hotspots sensitive to a specific OAM state to elevated temperature above the melting threshold and introduce a photothermal deformation to become shorter nanorods. During the decoding process, TPL emitted from the GNRs is based on nonlinear absorption that is proportional to fourth power of electric field amplitudes inside the nanoparticles. Therefore, TPL can provide enlarged difference and enhanced sensitivity for subtle changes in linear absorption, which can be used as an intuitive indication of the synthetic HD in individual GNRs.

Once a population of GNRs is photothermally deformed by an OAM beam with specific topological charge, polarization and wavelength, i.e. the optical encoding process mentioned in Experimental Methods, the TPL intensities between the case of low power decoding OAM beam and the cases of OAM beams with other combinations of topological charge, polarization and wavelength can show a clear TPL contrast and faithfully retrieve the encoded information (Fig. 3f). The OAM sensitive photothermal deformation and TPL signal form the kernel for six-dimensional optical encoding and decoding (Fig. 3, j-l). The encoded multichannel information is stable as the gold nanoaggregates are embedded in the polyvinyl alcohol matrix.

Supplementary notes 4. Definition of the similarity factor

A similarity factor can be defined to evaluate the quality of six-dimensional optical encryption among different channels: $S = \sum O_{mn}^{\ell,\lambda,P} \odot D_{mn}^{\ell,\lambda,P} / N$, where $O_{mn}^{\ell,\lambda,P}$ is the original binary information, $D_{mn}^{\ell,\lambda,P}$ is the decoded information regarding to different topological charge ℓ, polarization P and wavelength λ, m and n can be referred to the corresponding spatial positions of all multiplexing units in horizontal and vertical directions, respectively. The summation in the numerator accounts for the number N of '0' in the original binary information, where the OAM laser beam introduces a change in the localized HD through OAM-sensitive deformation of a population of GNRs. $\odot$ represents the operation of *xnor*.

Supplementary Figs. S1 to S15

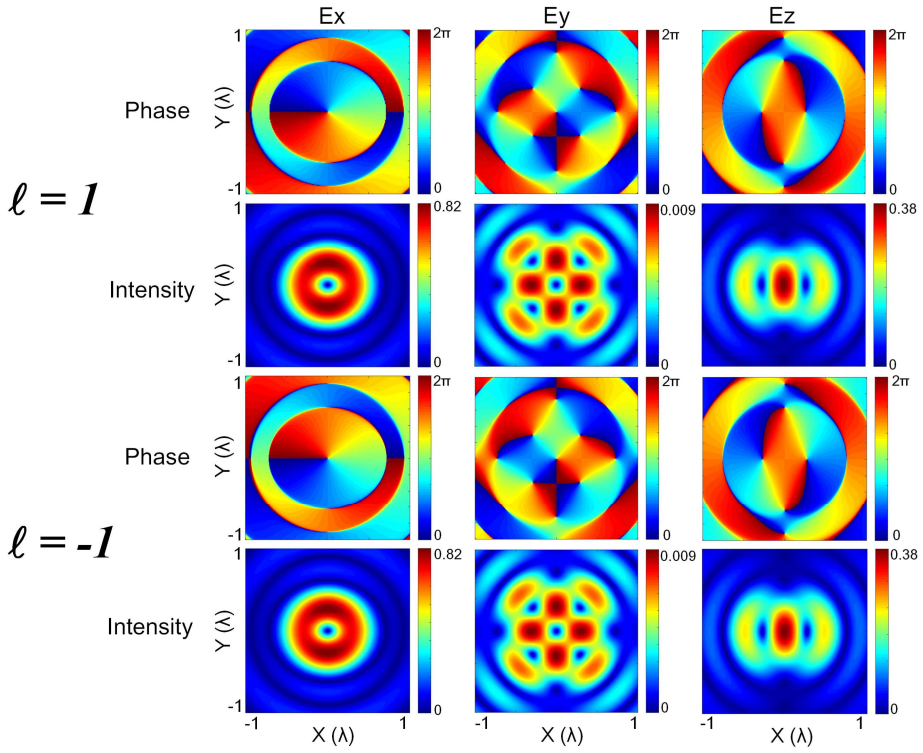

Supplementary Fig. S1 | Distributions of electric field intensity and phase for tightly focused OAM beams with different topological charges. The electric field intensity ($|E_x|^2$, $|E_y|^2$ and $|E_z|^2$) and phase distributions of tightly focused OAM beams with $\ell = \pm 1$ in the focal plane are shown. The working wavelength is 800 nm and the NA and magnification factor of the objective lens are 1.4 and 100×, respectively.

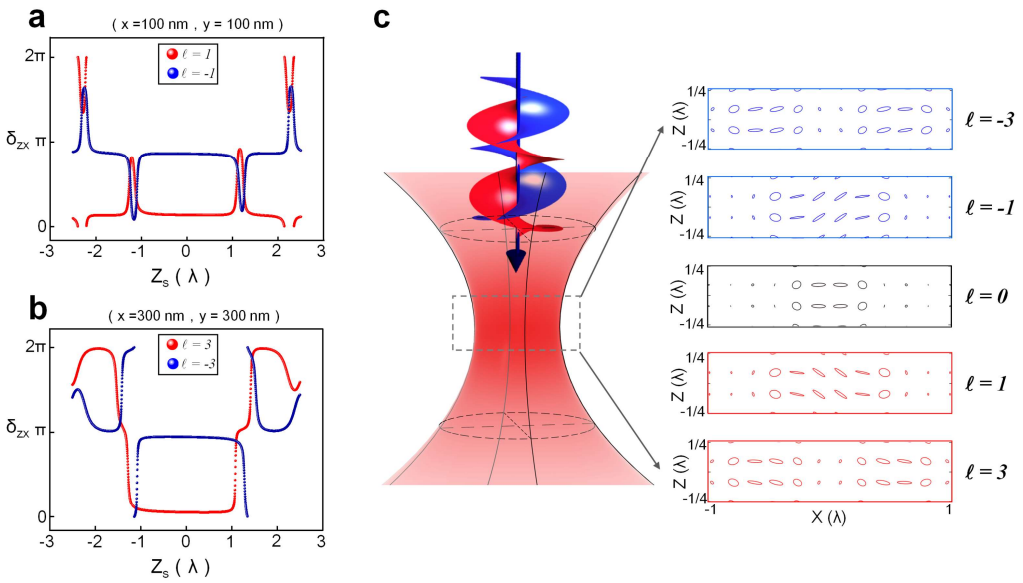

Supplementary Fig. S2 | The OAM associated Gouy phase differences and the corresponding polarization ellipses. Gouy phase differences between the components of E_z and E_x along the directions of transmission with different ℓ values ($\ell = \pm 1$ and $\ell = \pm 3$) are shown in (**a**) and (**b**). The corresponding X and Y positions are indicated in the insets. **c**, Corresponding polarization ellipse of tightly focused OAM beams with $\ell = \pm 1$ and $\ell = \pm 3$ at the X-Z plane are plotted. For comparison, the case for $\ell = 0$ is also shown. The spatial rotations of polarization ellipses clearly reveal the OAM dependence. The working wavelength is 800 nm and the NA and magnification factor of the objective lens are 1.4 and 100×, respectively.

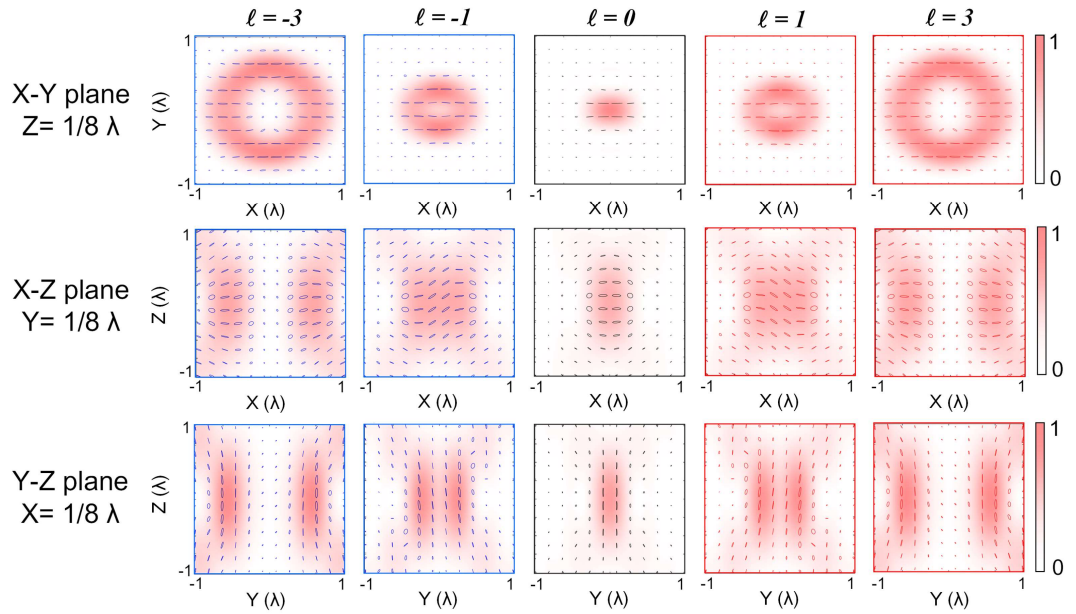

Supplementary Fig. S3 | Polarization ellipse governed by OAM of light. Polarization ellipses of tightly focused OAM beams with $\ell = \pm 1$, $\ell = \pm 3$ and $\ell = 0$ at *X*-*Y*, *X*-*Z* and *Y*-*Z* planes (shifted λ/8 from the focal centre) are presented, respectively. The working wavelength is 800 nm and the NA and magnification factor of the objective lens are 1.4 and 100×, respectively.

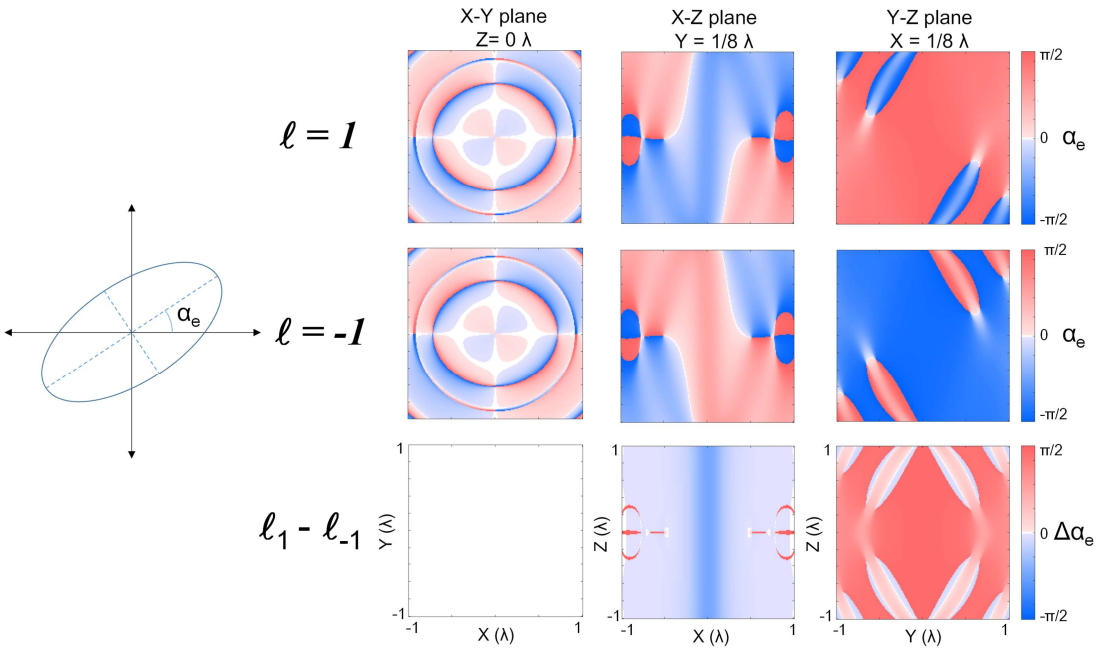

Supplementary Fig. S4 | Inclination angle difference of polarization ellipses for OAM beams with opposite topological charges. Ellipse inclination angle (α_e) of tightly focused OAM beams with $\ell = \pm 1$ and inclination angle difference (ℓ_1 - ℓ_{-1}) are shown at *X*-*Y*, *X*-*Z* and *Y*-*Z* planes (shifted λ/8 from the focal centre). Here, the ellipse inclination angle is defined as the tilted angle of the polarization ellipse with respective to the *X* or *Y* axis, as shown in the left inset.

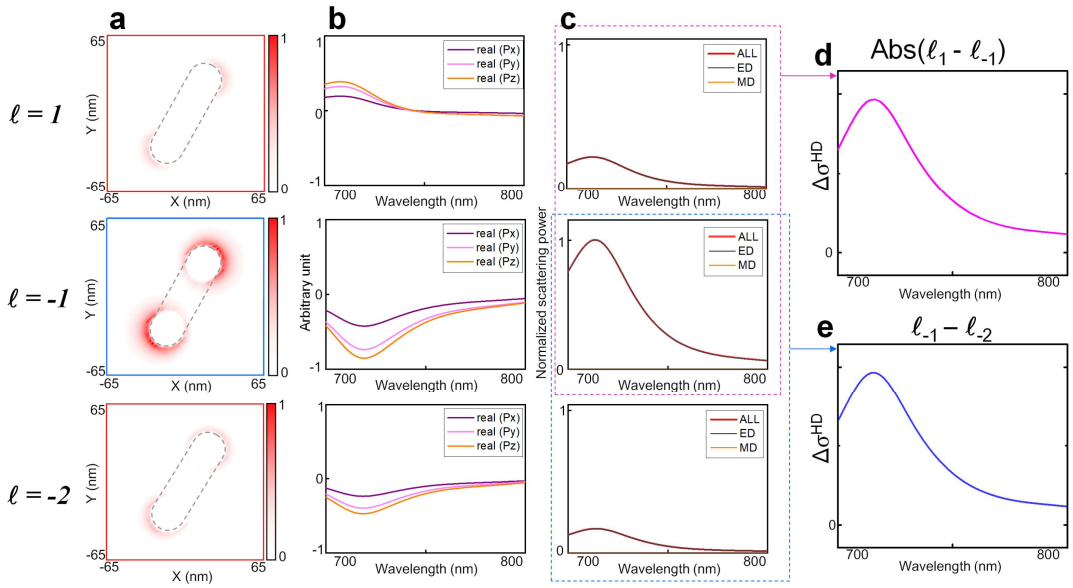

Supplementary Fig. S5 | Synthetic helical dichroism induced by OAM-dependent polarization ellipse. a, Simulated electric field intensity of a single gold nanorod, whose position is $Y = 280$ nm, $X = Z = 0$ nm, $\varphi = 45^{\circ}$, $\theta = 60^{\circ}$, under the excitation of tightly focused OAM beams with $\ell = \pm 1$ and $\ell = -2$, as schematically shown in Fig. 1d. The real part of induced electric dipoles and the corresponding electromagnetic multipolar decomposition of the nanoparticle are plotted in (**b**) and (**c**), respectively. (**d**) and (**e**) present the corresponding helical dichroism of nanoparticle under the excitation of OAM beams with different combinations of topological charges of ℓ_1 - ℓ_{-1} and ℓ_{-1} - ℓ_{-2}.

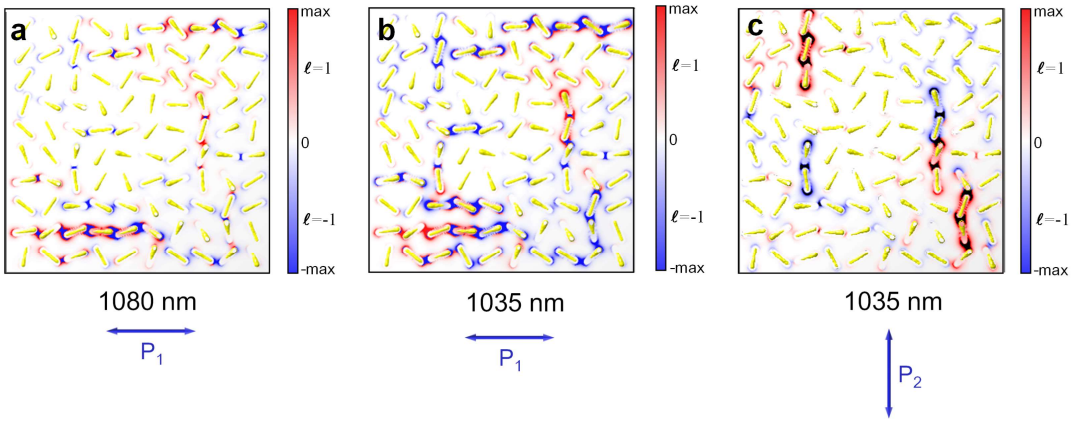

Supplementary Fig. S6 | Electric field intensity distributions of a 10 × 10 disorder GNR array under the excitations of different tightly focused OAM beams. a, The superposition of simulated electric field intensity under the excitations of OAM beams with opposite topological charges ($\ell = \pm 1$) and the horizontal polarization (p_1) at the wavelength λ = 1080 nm. Similar results for other combinations of wavelength and polarization are shown in (**b**) and (**c**), as indicated in the insets. Here, red and blue colors both represent the maxima of electric field intensity for opposite topological charges while white color indicates zero intensity. The coupled disorder GNRs are also superimposed in the figures. The GNR array is the same as the one presented in Fig. 2a. As can be seen, different combinations of topological charge, polarization and wavelength of the tightly focused OAM beam will excite distinct OAM-sensitive hotspots in the coupled disordered GNR array, resulting in the HD with polarization and wavelength sensitivity.

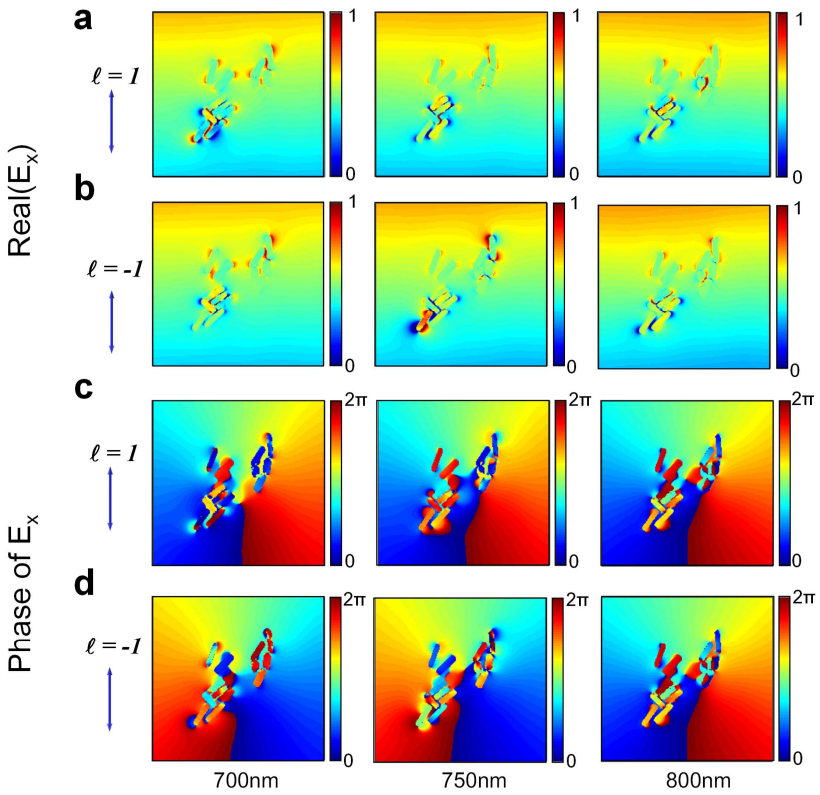

Supplementary Fig. S7 | Electric field distributions of an exemplary GNR assembly under the excitations of different tightly focused OAM beams. (**a**) and (**b**) show the real E_x of the array at the center plane of the structure under the excitations of tightly focused OAM beams with different combinations of wavelength and topological charge while fixing the linear polarization (blue double arrows) while (**c**) and (**d**) present the corresponding local phase of E_x, respectively. The GNR array is the same as the one presented in Fig. 3a. As can be seen from these figures, the excitations of OAM beams with opposite topological charges and different wavelengths result in distinct OAM-sensitive hotspots in this exemplary GNR assembly.

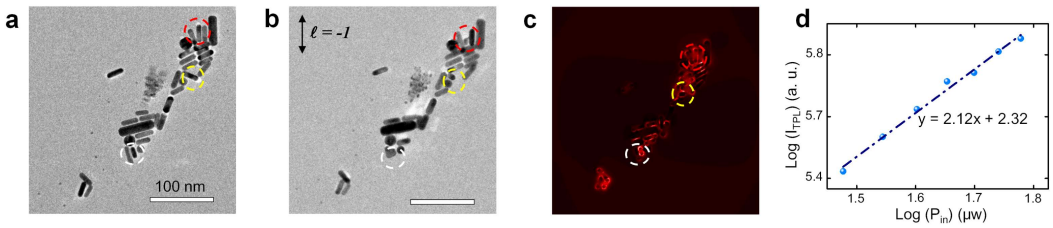

Supplementary Fig. S8 | Optical encoding process in disordered coupling GNRs by OAM beams. TEM images of the GNR assembly on copper mesh before (**a**) and after (**b**) the irradiation of femtosecond laser pulses (ℓ = -1, λ = 800 nm, NA = 0.75 and 20 ×) with an average power of 1000 μw and an exposure time of 25 ms. The scale bar is 100 nm and the polarization and topological charge are indicated in (**b**). **c**, Simulation result of the electric amplitude distribution for the structure shown in (**a**) under the excitation of the same tightly focused OAM beam used in experiment. The deformed GNRs and OAM-sensitive hotspots are outlined by dashed circles. Tightly focused OAM beam with certain combinations of topological charge, wavelength and polarization can selectively deform a portion of GNRs exhibiting HD. As a consequence, the deformation of such GNRs leads to a reduced TPL signal in the corresponding decoding channel. **d,** Dependence of the luminescence intensities on the excitation pulse powers plotted in a double-logarithmic scale and the slope is extracted to be 2.1243 which confirms the two-photon nature of the excitation. The TPL is integrated over a wavelength range from 420 nm to 690 nm.

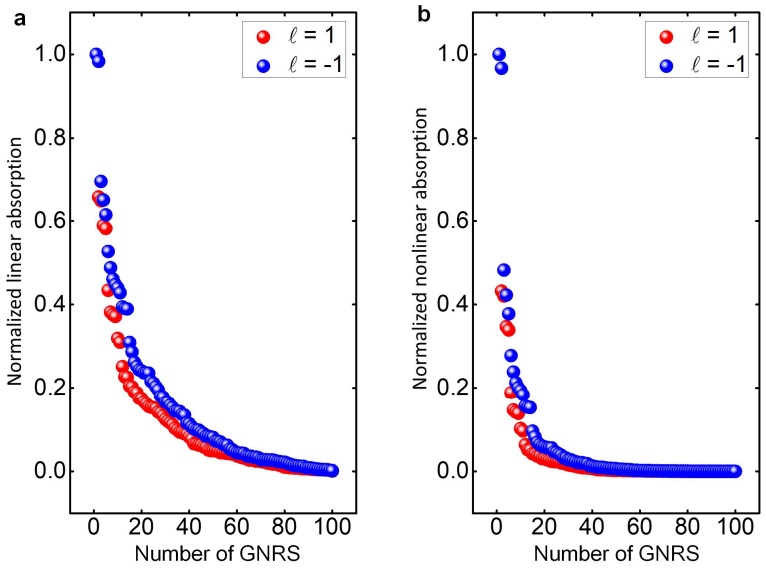

Supplementary Fig. S9 | Statistical results of normalized linear and nonlinear optical absorption of all GNRs in the disordered array. a, Statistical distributions of the normalized linear optical absorption of 100 GNRs shown in Fig. 2a under the excitations of tightly focused OAM beams with opposite topological charges near the resonant enhanced HD shown in Fig. 2b. The GNRs near the first few OAM-sensitive hotspots which exhibit the strongest field enhancements overwhelmingly contribute to the total amount of absorption of the array. As can be seem from this figure, the linear optical absorption is dominated by several highly excited GNRs in the array. For example, the first eight GNRs contribute more than 35% of linear optical absorption of the array. Owing to the nature of the biquadratic dependence of two-photon absorption on the electric field amplitude, such ratio can be further enhanced by utilizing nonlinear two-photon optical absorption of the array, where the first eight GNRs contribute more than 73% of total nonlinear absorption, as shown in (**b**). The NA and magnification of the objective lens used in simulation are 1.4 and 100 ×, respectively.

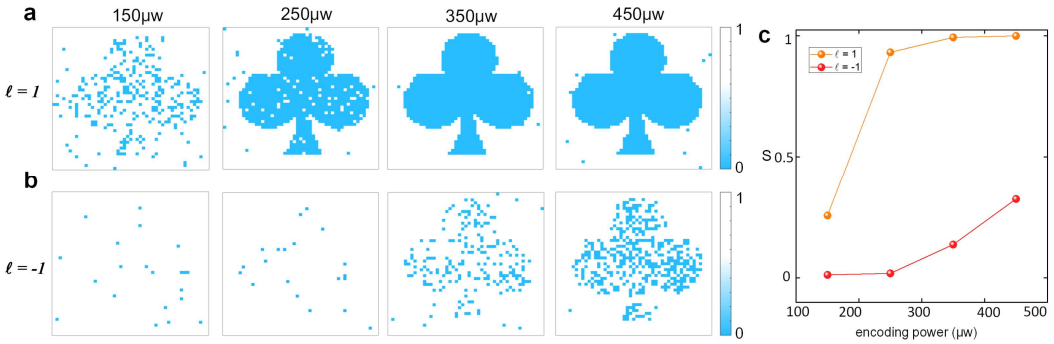

Supplementary Fig. S10 | Optical encoding power optimization for mitigating crosstalks between OAM beams with different topological charges. The encoded image is patterned by an OAM beam (ℓ = 1) with different recording laser powers. The corresponding decoded results through TPL signals are shown in (**a**). They are also decoded by the OAM beam with a different topological charge (ℓ = -1), where the results are shown in (**b**). The decoding power for all figures is 70 μW. The wavelength of the OAM beam is 800 nm and the horizontal polarization is used. The size of images is 40 × 40 μm^2 (2500 multiplexing units). The similarity factors *S* between decoded and target images for different encoding powers are presented in (**c**). As can be seen from this figure, there is an optimized encoding power to maximize the contrast between the encoding and decoding channels using different topological charge. By optimizing the writing powers to deform only the first few GNRs exhibiting the strongest contributions to the HD of specific OAM states, the decoding crosstalks with a suitable threshold to digitalize the signal between different OAM beams can be mitigated enormously.

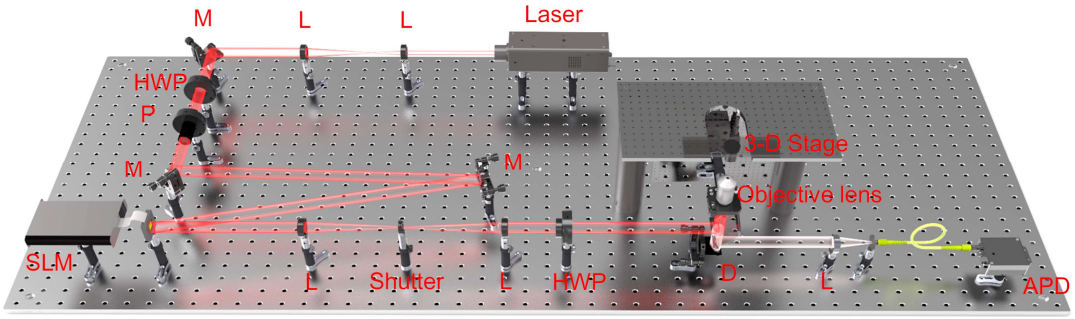

Supplementary Fig. S11 | Experimental setup for the six-dimensional optical encoding. L: lens, M: reflection mirror, HWP: half-wavelength plate, P: linear polarizer, SLM: spatial light modulator, D: dichroic mirror, 3-D Stage: three-dimensional stage, APD: avalanche photodiode. Details regarding experiment setup can be found in the Methods section.

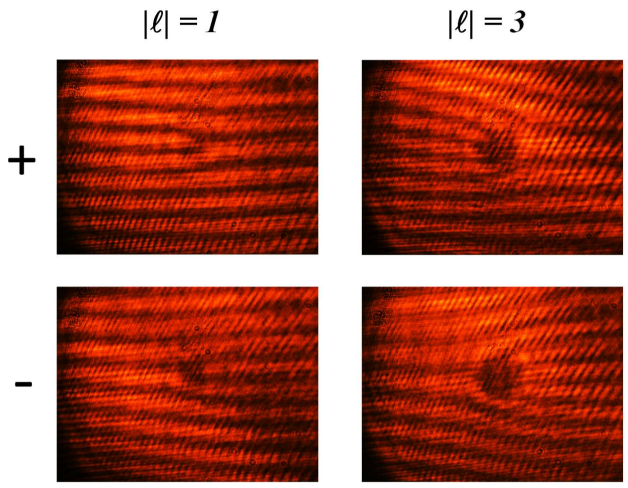

Supplementary Fig. S12 | Interference patterns between a collimated beam and the OAM carrying beams with different topological charges. The OAM beams used in the multiplexing experiments are checked by the interference patterns. Experimentally measured interference patterns for the $\ell = +n$ (top) and $\ell = -n$ (bottom) beams with different topological charges, $n = 1$ and 3, respectively.

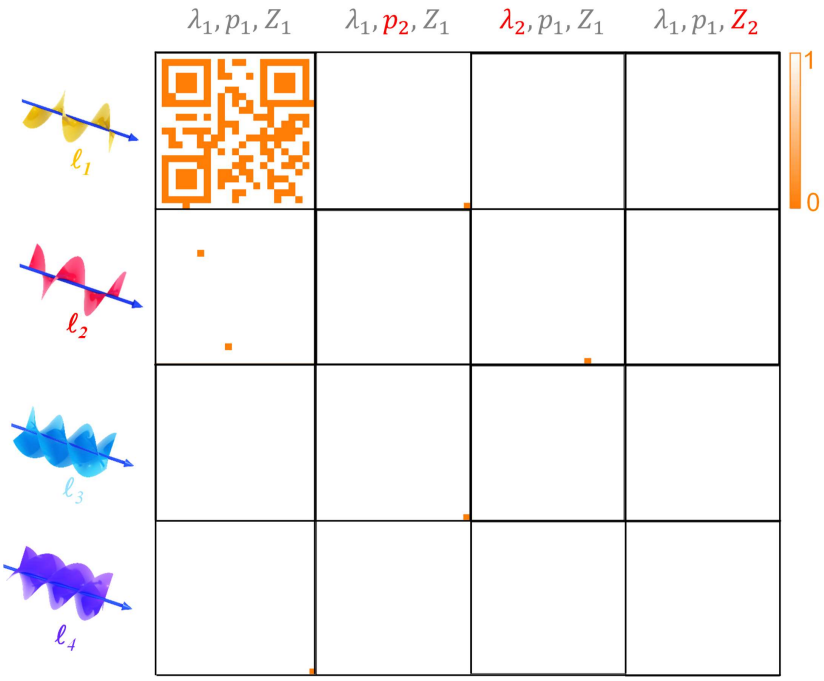

Supplementary Fig. S13 | Six-dimensional optical encryption. Optical encryption using OAM beams with distinct combinations of topological charges ($-\ell_1 = \ell_2 = 1$ and $-\ell_3 = \ell_4 = 3$), wavelengths ($\lambda_1 = 800$ nm, $\lambda_2 = 860$ nm) and linear polarizations (p_1 and p_2 are horizontal and vertical polarization, respectively) and Z locations ($Z_1 - Z_2 = 1$ μm). We encode the QR code utilizing a tightly focused OAM beam with a specified combination of topological charge (ℓ), wavelength (λ), polarization (p) and position (Z). The encoding power is 250 μw and the readout power is 70 μW. The encoding area is 32×32 μm^2 (27×27 encryption units, the pixel size is approximately 1.2 μm). As can be seen in this figure, the encrypted image can only be distinctively retrieved back using the OAM beam with identical ℓ_1-λ_1-P_1-Z_1 to the encoding beam while the demultiplexing cases utilizing other combinations of topological charge, wavelength, polarization and Z-position cannot retrieve the encoded information, as shown in the figure. According to the similarity factor S of all the sixteen cases evaluated in Fig. 4b, the proposed six-dimensional encryption resembles a secure optical encryption method. The encryption and decryption powers are 250 μW and 70 μW (450 μW and 120 μW) for $\ell = \pm 1$ ($\ell = \pm 3$).

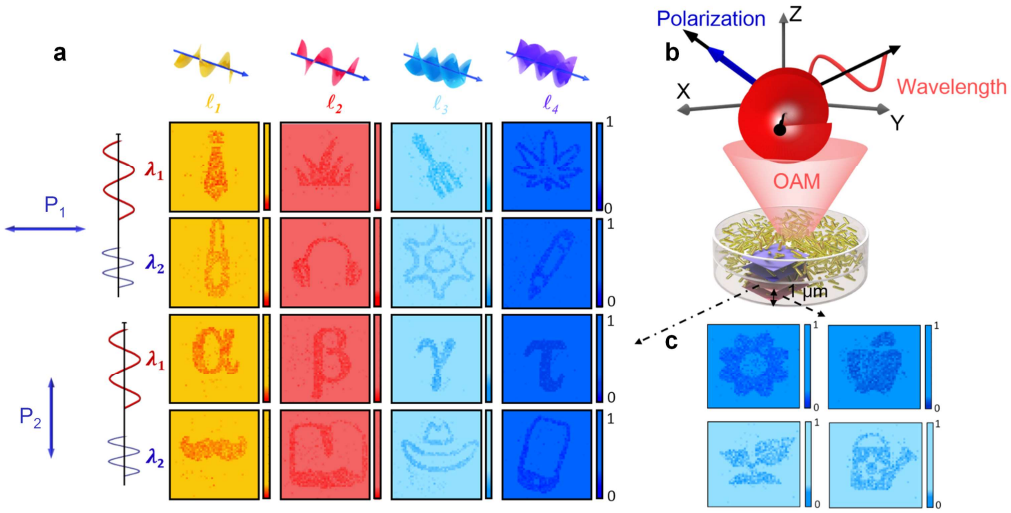

Supplementary Fig. S14 | Retrieved six-dimensionally encoded images. **a,** Optically encoding and decoding of sixteen images in the coupled disordered GNRs multiplexed at a *X*-*Y* plane beneath that shown in Fig. 4 at $Z = 2$ μm, as indicated by two bottom layers in the schematic (**b**). Four OAMs ($-\ell_1 = \ell_2 = 1$ and $-\ell_3 = \ell_4 = 3$), two linear polarizations (horizontal and vertical) and two wavelengths ($\lambda_1 = 800$ nm and $\lambda_2 = 860$ nm) are used. **c,** Examples of four of another 16 images are multiplexed and demultiplexed in a *X*-*Y* plane at $Z = 3$ μm. The size of all images is 60×60 μm^2 (50×50 multiplexing units). The recording and readout powers are 250 μW and 70 μW (450 μW and 120 μW) for $\ell = \pm 1$ ($\ell = \pm 3$).

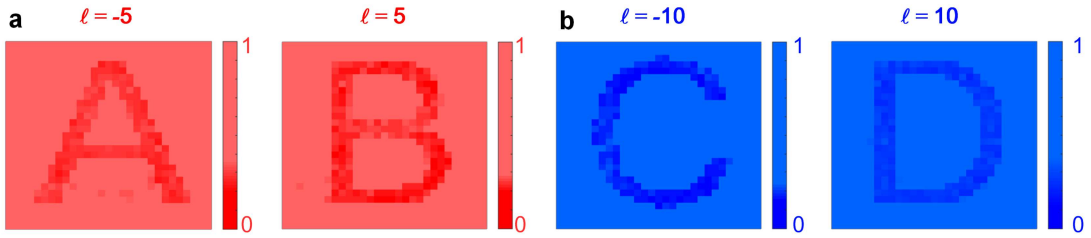

Supplementary Fig. S15 | Feasibility of physically-unbounded OAM state multiplexing. Optically encoding and decoding of four images at the same *X*-*Y* plane utilizing OAM beams with topological charges ($|\ell| = 5$) (**a**) and topological charges ($|\ell| = 10$) (**b**). The size of the image is 90 × 90 μm^2 (30 × 30 multiplexing units). The recording and readout powers are 700 μW and 200 μW (1400 μW and 350 μW) for $\ell = \pm 5$ ($\ell = \pm 10$).

Reference:

1. Kerber, R. M., Fitzgerald, J. M., Oh, S. S., Reiter, D. E. & Hess, O. Orbital angular momentum dichroism in nanoantennas. *Commun. Phys*. **1**, 87 (2018).